

10^4 , is about three times as large as the measured atom number in the soliton, it is likely that during the 50 ms phase where a is changed from 0 to negative values, one or several collapses occur until the critical number for a stable BEC is reached. Indeed, the collapse time constant is predicted to be much less than 50 ms for our experimental conditions (21). During the transfer into the 1D waveguide, the BEC is transformed into a soliton and the noncondensed cloud is clearly observed at guiding times up to 6 ms as a broader background distribution. Nonadiabatic projection of the BEC from the confining onto the expulsive potential is expected to play a negligible role here, according to numerical simulations (22). At longer times, the noncondensed atoms spread apart and become undetectable. Thus, during the propagation phase the soliton decouples itself from the noncondensed fraction, resulting in a nearly pure soliton.

Finally, removal of the expulsive axial potential will allow us to extend the stability domain toward lower values of $N|a|$ and

longer observation times. The soliton size could then be measured in situ, as well as its lifetime. The study of coherence properties of solitons and of binary collisions between solitons is an immediate extension of the present work.

References and Notes

- See, for example, the recent special issue: *Chaos* **10**, 471 (2000).
- P. A. Ruprecht, M. J. Holland, K. Burnett, M. Edwards, *Phys. Rev. A* **51**, 4704 (1995).
- C. C. Bradley, C. A. Sackett, R. G. Hulet, *Phys. Rev. Lett.* **78**, 985 (1997).
- J. L. Roberts *et al.*, *Phys. Rev. Lett.* **86**, 4211 (2001).
- V. E. Zakharov, A. B. Shabat, *Sov. Phys. JETP* **34**, 62 (1972).
- V. M. Pérez-García, H. Michinel, H. Herrero, *Phys. Rev. A* **57**, 3837 (1998).
- L. D. Carr, M. A. Leung, W. P. Reinhardt, *J. Phys. B* **33**, 3983 (2000).
- S. Burger *et al.*, *Phys. Rev. Lett.* **83**, 5198 (1999).
- J. Denschlag *et al.*, *Science* **287**, 97 (2000).
- E. Tiesinga, B. J. Verhaar, H. T. S. Stoof, *Phys. Rev. A* **47**, 4114 (1993).
- V. Venturi, C. Williams, personal communication.
- M.-O. Mewes, G. Ferrari, F. Schreck, A. Sinatra, C. Salomon, *Phys. Rev. A* **61**, 011403R (2000).
- F. Schreck *et al.*, *Phys. Rev. A* **64**, 011402R (2001).
- F. Schreck *et al.*, *Phys. Rev. Lett.* **87**, 080403 (2001).
- See, for instance, R. Grimm, M. Weidemüller, Y. B. Ovchinnikov, *Adv. At. Mol. Opt. Phys.* **42**, 95 (2000).
- S. Inouye *et al.*, *Nature* **392**, 151 (1998).
- J. L. Roberts, N. R. Claussen, S. L. Cornish, C. E. Wieman, *Phys. Rev. Lett.* **85**, 728 (2000).
- M. D. Barrett, J. A. Sauer, M. S. Chapman, *Phys. Rev. Lett.* **87**, 010404 (2001).
- In the vertical direction, a residual astigmatism of the imaging system gives a resolution limit of 16 μm .
- Over this distance, the change in magnetic field due to the curvature is 0.1 G, and therefore the change in the scattering length is negligible (Fig. 2).
- Y. Kagan, A. E. Muryshev, G. V. Shlyapnikov, *Phys. Rev. Lett.* **81**, 933 (1998).
- L. D. Carr, Y. Castin, in preparation.
- We are grateful to K. Corwin, M. Olshanii, G. Shlyapnikov, C. Williams, V. Venturi, and B. Esry for important contributions to this work and to J. Dalibard and C. Cohen-Tannoudji for useful discussions. Supported by the DAAD (F.S.), the European Union network CT 2000-00165 CAUAC (G.F.), and the NSF MPS-DRF 0104447 (L.D.C.). This work was supported by CNRS, Collège de France and Région Ile de France. Laboratoire Kastler Brossel is Unité de recherche de l'Ecole Normale Supérieure et de l'Université Pierre et Marie Curie, associated with CNRS.

19 February 2002; accepted 5 April 2002

Electrochemistry and Electrogenerated Chemiluminescence from Silicon Nanocrystal Quantum Dots

Zhifeng Ding,¹ Bernadette M. Quinn,¹ Santosh K. Haram,¹ Lindsay E. Pell,² Brian A. Korgel,^{2*} Allen J. Bard^{1*}

Reversible electrochemical injection of discrete numbers of electrons into sterically stabilized silicon nanocrystals (NCs) (~ 2 to 4 nanometers in diameter) was observed by differential pulse voltammetry (DPV) in N,N' -dimethylformamide and acetonitrile. The electrochemical gap between the onset of electron injection and hole injection—related to the highest occupied and lowest unoccupied molecular orbitals—grew with decreasing nanocrystal size, and the DPV peak potentials above the onset for electron injection roughly correspond to expected Coulomb blockade or quantized double-layer charging energies. Electron transfer reactions between positively and negatively charged nanocrystals (or between charged nanocrystals and molecular redox-active coreactants) occurred that led to electron and hole annihilation, producing visible light. The electrogenerated chemiluminescence spectra exhibited a peak maximum at 640 nanometers, a significant red shift from the photoluminescence maximum (420 nanometers) of the same silicon NC solution. These results demonstrate that the chemical stability of silicon NCs could enable their use as redox-active macromolecular species with the combined optical and charging properties of semiconductor quantum dots.

In a bulk semiconductor, electrons and holes move freely throughout the crystal. However, in a nanocrystal, confinement of the electrons and holes leads to a variety of optical and electronic consequences, including size-dependent molecular-like optical properties, greater electron/hole overlap for enhanced photoluminescence (PL) efficiencies, and discrete single-electron/hole charging. Because of their

enormous surface area-to-volume ratios, nanocrystals (NCs) are highly susceptible to heterogeneous redox chemistry with the surrounding environment. Depending on the semiconductor and the surface chemistry, this chemical reactivity can lead to either fatal chemical degradation or new useful properties, such as reversible photocatalytic and electrochromic properties and redox reactivity.

Semiconductor NCs have been prepared with narrow size distributions, controlled surface chemistry, and internal bulk crystal structure (1, 2), and adsorbed capping ligands are often used to control size and prevent irreversible aggregation. Although the electrochemical properties of monolayer-protected metallic NCs have been well documented (3, 4), reports concerning the electrochemical properties of semiconductor NCs remain scarce (5–9). Difficulties include the limited potential window available in aqueous solutions, the limited solubility of many NCs in nonaqueous solvents, and the need for highly pure, isolated, monodisperse dots. Compound semiconductor NCs, such as CdS, are also chemically unstable upon electron transfer. For example, CdS NCs are irreversibly oxidized and reduced when electron transfer occurs at an electrode (9). Elemental semiconductor NCs, such as Si and Ge, should be more stable. Here we show that monolayer-protected Si NCs are chemically stable upon electron and hole injection; furthermore, electron/hole annihilation through electron transfer reactions between NCs, or NCs with redox-active coreactants, leads to visible light production [electrogenerated chemiluminescence (ECL)].

We recently developed a new synthetic strategy to produce Si NCs terminated with a

¹Department of Chemistry and Biochemistry, ²Department of Chemical Engineering, Center for Nano- and Molecular Science and Technology, Texas Materials Institute, The University of Texas at Austin, Austin, TX 78712, USA.

*To whom correspondence should be addressed. E-mail: ajbard@mail.utexas.edu (A.J.B.); korgel@mail.che.utexas.edu (B.A.K.).

capping agent consisting of a combination of hydrogen and alkoxide, using solvents heated and pressurized above their critical points to temperatures between 350° and 500°C (10). These NCs are efficient emitters of visible light, with quantum yields between 5 and 20% and size-tunable color that can range from blue to red, different from H- or oxide-terminated samples in the same size range reported earlier. This efficiency is rather remarkable, given that the indirect band gap of bulk Si makes it a poor candidate for a light-emitting material. Although the precise origin of the light emission is

still unknown (11), quantum confinement in Si has led to efficient PL (12, 13), and radiative transitions have been observed (2) in a variety of Si nanostructures, including thin wires (14), dots (10), and porous Si (2, 15). For the experiments reported here, octanol-, octene- and octanethiol-capped Si NCs were prepared in supercritical cyclohexane according to the methods described in (10). The Si NCs are readily soluble in a variety of organic solvents, including those used here: *N,N'*-dimethylformamide (DMF) and acetonitrile (MeCN).

The electrochemical properties of freely

diffusing Si NCs dispersed in nonaqueous organic solvents were measured at a Pt electrode (16). Discrete steps associated with single-electron charging and a large central gap between the onset of oxidation and reduction, characteristic of the energy difference between the highest occupied and lowest unoccupied molecular orbitals (the HOMO-LUMO gap), were observed. Typical electrochemical responses for different solutions of Si NCs are given in Fig. 1, with NC sizes of (i) 2.77 ± 0.37 , (ii) 2.96 ± 0.91 , and (iii) 1.74 ± 0.67 nm. For example, in Fig. 1A, there are as many as five well-resolved differential pulse voltammetry (DPV) peaks between 0 and -2.1 V. These regularly spaced peaks are reversible and highly reproducible. The observed response was stable on repetitive potential cycling over long time periods, with no evidence of fouling or film formation on the Pt electrode surface.

This DPV response is analogous to that observed by Murray and co-workers (3) for thiol-capped metal clusters, who introduced the term quantized double-layer charging to differentiate this collective electrochemical response from Coulomb blockade phenomena observed for single-charge injection to isolated individual dots in scanning tunneling microscopy (STM) experiments, also called "addition spectra" (17). Unlike the electrical response measured by STM, the electrochemical response is limited by quantum dot diffusion to the electrode surface. Nonetheless, the charging energy μ_i required for electron or hole addition is the same for STM and DPV measurements. For example, we recently observed an electrochemical Coulomb staircase based on two nanometer-sized electrodes connected in series through a solution containing a redox couple (18).

The small size of the NCs causes electron addition to be quantized. The charging energy required to add the first electron μ_1 equals the electron quasiparticle energy ϵ_{e1} , which depends on the size-dependent shift in the LUMO ϵ_{e1}^0 and the electron "self-energy" Σ_{e1} , which results from its image charge in the surrounding dielectric media: $\epsilon_{e1} = \epsilon_{e1}^0 + \Sigma_{e1}$. Calculated values of Σ_{e1} typically range from 0.2 to 0.5 eV for Si nanocrystals in the size range studied here (19). A second electron must also overcome the electron-electron Coulomb interaction $J_{e1,e2}$ within the particle to add to a negatively charged NC, $\Delta_{1,2}^{(e)} = \mu_2 - \mu_1 = J_{e1,e2}$. For Si dots, the calculated ϵ_{e1} values are almost entirely determined by Coulomb energies, because the six lowest-energy conduction levels are very close in energy. A classical estimation of $J_{e1,e2} \approx e^2/2C_{NC}$ reveals that the sub-attofarad (aF) capacitances for NCs give rise to $\Delta_{1,2}^{(e)} \gg k_B T$ even at room temperature, leading to discrete charging events in the DPV scans (3, 8, 18, 20). If C_{NC} is independent of the

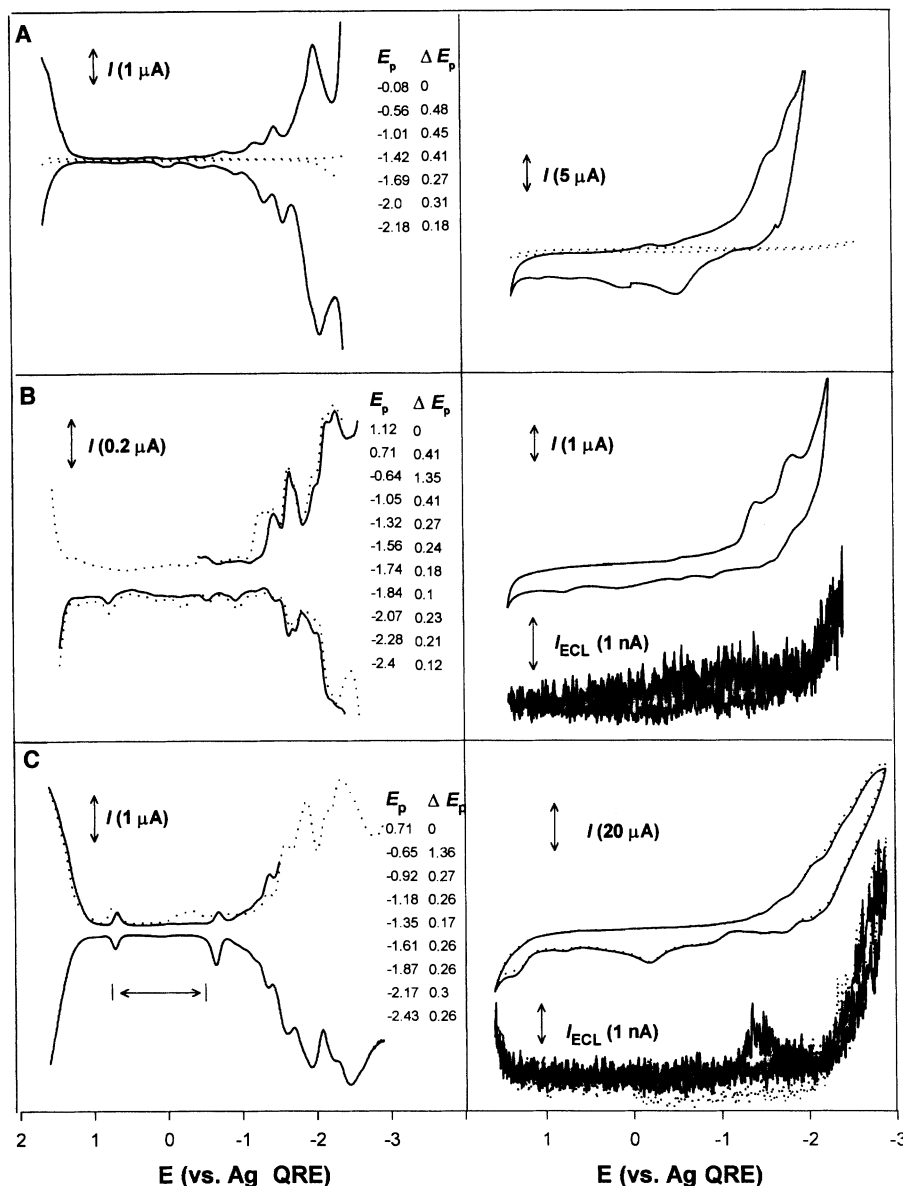
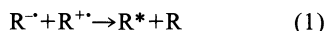


Fig. 1. Cyclic voltammograms (right panels) and differential pulse voltammograms (left panels) for several batches of Si nanoparticles in 0.1 M tetrahexylammonium perchlorate (THAP) DMF solution. I , current; E_p , current peak potential, ΔE_p , potential difference between two succeeding peaks; I_{ECL} , ECL photocurrent from the photomultiplier tube; QRE, quasi-reference electrode. The NC's size and dispersion were (A) 2.77 ± 0.37 , (B) 2.96 ± 0.91 , and (C) 1.74 ± 0.67 nm. Cyclic voltammetric ECL voltage curves are plotted in (B) and (C). The dotted curves in (A) represent the response of the blank supporting electrolyte solution. The dotted curves in (B) and (C) are the responses for different initial DPV scan potentials.

number of electrons injected, consecutive charge injection should occur in regular potential steps, $\Delta V = e/C_{\text{NC}}$ (3, 18). Although the DPV peaks in Fig. 1 were not separated by exactly the same ΔV , the average $\Delta V \approx 0.4$ V corresponds to a capacitance of approximately 0.4 aF per cluster (Fig. 1A); this is comparable to the value reported for organic-capped noble metal clusters (4). The ΔV compares favorably with values reported for organic-capped Au nanocrystals and with recent calculations by Franceschetti and Zunger (19) for Si quantum dots with $\Delta_{1,2}^{(e)}$ on the order of ~ 0.4 to 0.6 eV. With increasing NC charge, ΔV decreased measurably, perhaps because of multielectron effects or NC size dispersity, which can smear the observed responses shown in Fig. 1, A and B (4). The electrochemical behavior seen in these figures was very sensitive to the NC size variation (± 0.37 nm in Fig. 1A and ± 0.91 nm in Fig. 1B).

The DPV responses in Fig. 1 are from differently sized NCs. Common features include the appearance of a large central gap ($\mu_1 - \mu_{-1} > 1.3$ V; the subscript “-1” refers to the hole chemical potential) and the general absence of DPV peaks in the positive potential region. This last feature was not a limitation of the available electrochemical window, as seen in Fig. 1A, where the DPV response in the absence of Si NCs is given. Electron injection occurred as discrete charging events; however, NC oxidation (hole injection) was not generally quantized although calculations suggest that it should be (19), and the DPV response was characterized by a continuous increase in current with potential indicative of multiple charge transfers. Nevertheless, the forward and reverse DPV scans are relatively symmetric, indicating that both single and multiple charge transfers are reversible. For comparable CdS and PbS NCs (7, 9), electrochemical electron and hole injection were irreversible and multielectron transfer processes were proposed; that is, the injected charge was consumed by fast coupled chemical reactions due to cluster decomposition. The large size-dependent central gap relates to the energetic difference (the HOMO-LUMO gap) (3), reflecting the quantized electronic structure of the semiconductor NC (19): $\mu_1 - \mu_{-1} = \epsilon_{e1}^0 - \epsilon_{h1}^0 + \sum_{e1} + \sum_{h1}$. The optical gap $\epsilon_{\text{gap}}^{\text{opt}}$, however, relates to ϵ_{e1}^0 , ϵ_{h1}^0 and the electron-hole Coulomb interaction $J_{e1,h1}$: $\epsilon_{\text{gap}}^{\text{opt}} = \epsilon_{e1}^0 - \epsilon_{h1}^0 - J_{e1,h1}$. Therefore, $(\mu_1 - \mu_{-1}) - \epsilon_{\text{gap}}^{\text{opt}} = \sum_{e1} + \sum_{h1} + J_{e1,h1}$. The HOMO-LUMO gap increases with decreasing NC size from 2.96 ± 0.91 nm in Fig. 1B to 1.74 ± 0.67 nm in Fig. 1C. However, this apparent electrochemical gap can be affected by the presence of nonpassivated surface states that can act as local traps for electrons and holes. We estimate that 30 to 50% of the surface of the NC may be ligand-free and coated with a mixture of H, Si-C = O and possibly a small amount of oxide (10).

Light emission by charge injection, or ECL, into freely diffusing NCs occurred under repetitive electrode potential cycling (as in Fig. 1, B and C) or pulsing (Fig. 2) between NC oxidation and reduction. In ECL experiments, electron-transfer annihilation of electrogenerated anion and cation radicals results in the production of excited states (20, 21)



In this case, $R^{\cdot-}$ and $R^{\cdot+}$ refer to negatively and positively charged Si NCs electrogenerated at the Pt electrode, which then react in solution to give the excited state R^* . ECL was not observed through an annihilation-type mechanism 1 for thioglycerol-capped CdS quantum dots (9) because of the instability of electrogenerated reactants. In order for ECL to occur through mechanism 1, the NCs must be chemically stable and maintain their charged states long enough to transfer charge upon colliding with oppositely charged NCs in solution. The relative ECL intensity was greater in the potential region where anionic NCs are electrogenerated (Figs. 1C and

2A), which may indicate that the electrogenerated oxidized forms are more stable. Light emission was not observed when the applied electrode potential was not sufficient to generate both the negatively and positively charged species. The ECL spectrum (Fig. 3A) obtained from the annihilation (Eq. 1) in MeCN, where the applied electrode potential was pulsed between the oxidation and reduction potentials (double potential step) in 100-ms steps (20, 21), showed a maximum at 640 nm.

Higher intensity light emission from the Si NC solution was observed when coreactants were added, which help overcome either the limited potential window of a solvent or poor radical anion or cation stability (20). For example, by adding excess $\text{C}_2\text{O}_4^{2-}$ to the NC solution (Fig. 2B), ECL only requires hole injection and can be obtained by simply oxidizing the NCs. In this case, the oxidation of oxalate produces a strong reducing agent, $\text{CO}_2^{\cdot-}$, which can inject an electron into the LUMO of an oxidized Si NC to produce an excited state that then emits light (Figs. 2B and 3B) (20, 22).

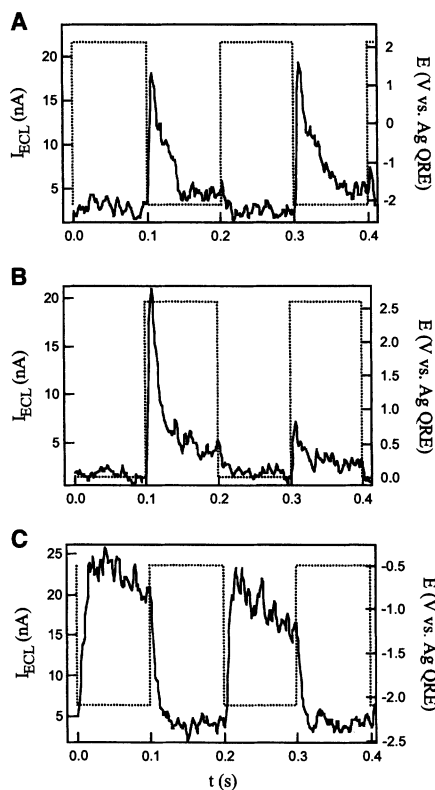
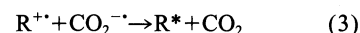


Fig. 2. ECL transients for (A) annihilation of cation and anion radicals in 0.1 M THAP MeCN solution, (B) an oxalate coreactant system with 2.5 mM tetrabutyl ammonium oxalate added to the solution of (A), and (C) a persulfate coreactant system in 0.1 M THAP DMF solution with 6 mM tetrabutylammonium persulfate added. The nanoparticles are ~ 2 to 4 nm in diameter. Dotted curves indicate applied potential steps; solid curves indicate ECL transients. t , time.

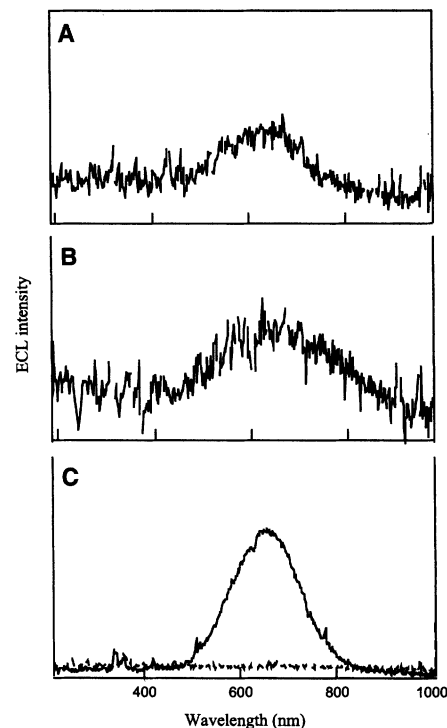
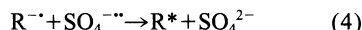


Fig. 3. ECL spectra for (A) annihilation of cation and anion radicals generated by stepping the potential between 2.7 and -2.1 V at 10 Hz with an integration time of 30 min in the same solution as in Fig. 2A; (B) an oxalate coreactant system, stepping the potential between 0.1 and 3 V at 10 Hz, integration time 40 min in the same solution as in Fig. 2B; and (C) a persulfate coreactant system, stepping the potential between -0.5 and -2.5 V at 10 Hz, integration time 10 min in the same solution as in Fig. 2C. The dotted curve in (C) is the ECL spectrum for the blank solution.

Similarly, ECL was observed in the potential region for NC reduction through the addition of excess $\text{S}_2\text{O}_8^{2-}$ to solution. Reduction of persulfate produces a strong oxidant, $\text{SO}_4^{\cdot-}$, which can then react with the negatively charged NCs by injecting a hole into the HOMO, producing an excited state (Figs. 2C and 3C) (23, 24)



A higher concentration of Si NCs was used for the persulfate measurements, which may account for the higher ECL intensity and lower decay rate apparent in Figs. 2C and 3C in comparison to Fig. 2, A and B, and Fig. 3, A and B. The solvent used may also play a role. After the ECL experiments, the solutions showed the same PL as the original solution, so no bulk degradation of the Si NCs occurred.

The ECL spectra in the above three cases all show a maximum wavelength of 640 nm, which is substantially red-shifted from that in the PL spectra (Fig. 4B). The orange ECL emission was not sensitive to NC size or the capping agent used. On the other hand, the Si NC PL is size-dependent (10). A few important observations and conclusions can be drawn from the ECL data. First of all, the electrochemical "turn-on voltage" (that is, the potential gap in Fig. 1, B and C) for radiative electron-hole annihilation between positive and negatively charged NCs exceeds the optical transition energy. This observation is consistent with electron and hole injection into separate NCs requiring greater energy than optical excitation. Second, the turn-on voltage for ECL significantly exceeds $\mu_1 - \mu_{-1}$. Although the potential difference $\mu_1 - \mu_{-1}$ enables electron and hole injection, and electron transfer between charged NCs in solution is possible, the carrier energies are not large enough to produce optically radiative electron-hole recombination. This observation is consistent with previous observations of Si NCs. Excitation energies for efficient PL significantly exceeded the absorption edge, with PL intensity

that depends sensitively on excitation energy, as shown in Fig. 4B, in which the excitation wavelength from top to bottom was between 360 and 520 nm at 20-nm intervals. The shift in peak position with excitation energy is unlikely to be caused by polydispersity, because the NCs were size-selected by column chromatography. Furthermore, the PL energy is considerably greater than the absorption edge, indicating that the lowest-lying energy levels do not result in strongly radiative transitions. Qualitatively, the ECL and DPV data are as expected for Si NCs.

Quantitatively, however, the energetic difference between the PL and ECL of approximately 0.8 eV is more difficult to understand and suggests that the emitting states are different. Previously, for Si NCs terminated with hydrogen atoms, the indirect band gap was reported to shift from the bulk value of 1.1 eV to ~2.1 eV for nanocrystals about 2 nm diameter, and the direct transition appeared to blue shift by 0.4 eV from its 3.4 eV bulk value over the same size range. In that case, violet PL (~365 nm) was the most intense emission and was attributed to direct electron-hole recombination, whereas other less intense PL peaks (~580 nm) were assigned to surface state and phonon-assisted recombination (11). Undoubtedly, ECL depends more sensitively on surface chemistry and the presence of surface states. PL mainly occurs through excitation and emission within the NC core, though the electron and hole wave functions can interact strongly with the NC surface. Despite a few notable exceptions (25, 26), charge injection in a Si nanocrystal is generally assumed to occur via its surface states, given the large surface area and the possible presence of many dangling bonds. If we consider the Si NC/oxalate coreactant system (Eq. 3) as an example, the Si cores have band gaps greater than the energy separation of the surface states. The core band gaps depend on the NC size, whereas the energy separation of the surface states is only slightly affected by the particle size (11, 27) (Fig.

4A). As the electrode potential is made more positive, holes are injected into the particle. Concurrently, oxalate is oxidized and undergoes a following chemical reaction generating the powerful reducing agent $\text{CO}_2^{\cdot-}$. This intermediate injects an electron across the particle surface (Eq. 3) and makes emission possible through surface electron-hole recombination. The other two ECL processes (Eqs. 1 and 4) are assumed to occur through a similar mechanism. The observed ECL emission insensitivity to core size and capping agent supports the surface state conjecture (11) and this proposed mechanism. Thus, the difference in light emission through PL and ECL from the same Si NCs most likely results from the greater significance of surface states for charge injection as opposed to photoexcitation. Similar long-wavelength emission is found with porous Si produced by anodic etching in the presence of organic surface modifiers (28).

These results reveal that NCs of the elemental semiconductor Si are more chemically robust than the compound semiconductor NCs studied to date. The Si NCs have the ability to store charge in solution, which can subsequently lead to light emission upon electron and/or hole transfer. This quality provides electrochemically sensitive optoelectronic properties that may find future use in new sensor technologies.

References and Notes

1. A. P. Alivisatos, *Science* **271**, 933 (1996).
2. S. S. Iyer, Y. H. Xie, *Science* **260**, 40 (1993).
3. S. Chen et al., *Science* **280**, 2098 (1998).
4. S. Chen, R. W. Murray, S. W. Feldberg, *J. Phys. Chem. B* **102**, 9898 (1998).
5. P. Hoyer, H. Weller, *Chem. Phys. Lett.* **224**, 75 (1994).
6. ———, *J. Phys. Chem.* **99**, 14096 (1995).
7. S. Chen, L. A. Truax, J. M. Sommers, *Chem. Mater.* **12**, 3864 (2000).
8. A. E. Hanna, M. T. Tuominen, M. Tinkham, *Phys. Rev. Lett.* **68**, 3228 (1992).
9. S. K. Haram, B. M. Quinn, A. J. Bard, *J. Am. Chem. Soc.* **123**, 8860 (2001).
10. J. D. Holmes et al., *J. Am. Chem. Soc.* **123**, 3743 (2001).
11. J. P. Wilcoxon, G. A. Samara, P. N. Provencio, *Phys. Rev. B Condens. Matter Mater. Phys.* **60**, 2704 (1999).
12. M. Nirmal, L. Brus, *Acc. Chem. Res.* **32**, 407 (1999).
13. D. Kovalev et al., *Phys. Rev. Lett.* **81**, 2803 (1998).
14. J. D. Holmes, K. P. Johnston, R. C. Doty, B. A. Korgel, *Science* **287**, 1471 (2000).
15. P. McCord, S. L. Yau, A. J. Bard, *Science* **257**, 68 (1992).
16. General experiments for electrochemistry (such as cyclic voltammetry and differential pulse voltammetry) and ECL of Si nanoparticles were done as follows: A cylindrical Pyrex vial 1.2 cm in diameter was used as an electrochemical cell, where a 1- or 2-mm Pt disk, Pt coil, and silver wire served as working, counter, and reference electrodes, respectively. The ECL signal was recorded on a charge-coupled device camera. ECL could also be measured by a photomultiplier tube and recorded as cyclic voltammetric ECL or ECL transients.
17. R. P. Andres et al., *Science* **272**, 1323 (1996).
18. F.-R. F. Fan, A. J. Bard, *Science* **277**, 1791 (1997).
19. A. Franceschetti, A. Zunger, *Phys. Rev. B Condens. Matter Mater. Phys.* **62**, 2614 (2000).
20. A. J. Bard, L. R. Faulkner, *Electrochemical Methods, Fundamentals and Applications* (Wiley, New York, ed. 2, 2001).

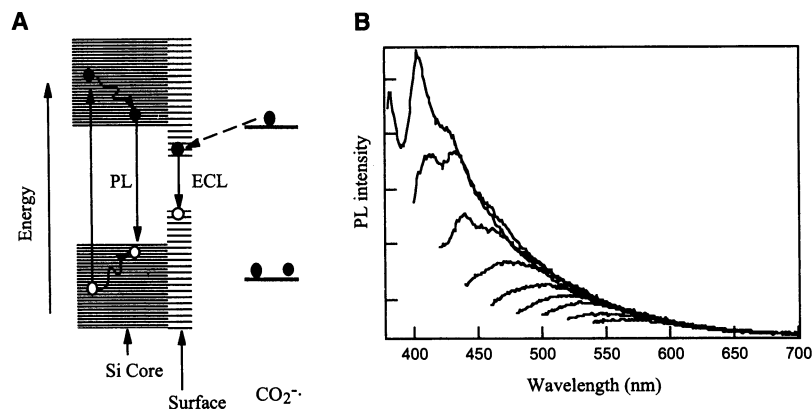


Fig. 4. (A) Schematic mechanisms for ECL and PL of Si clusters. (B) PL spectra at different excitation energies recorded with the same solution as in Fig. 2A. The excitation wavelength from top to bottom was between 360 and 520 nm at 20-nm intervals.

21. L. R. Faulkner, A. J. Bard, in *Electroanalytical Chemistry*, A. J. Bard, Ed. (Dekker, New York, 1977), vol. 20, pp. 1–95.
22. T. C. Richards, A. J. Bard, *Anal. Chem.* **67**, 3140 (1995).
23. H. S. White, A. J. Bard, *J. Am. Chem. Soc.* **104**, 6891 (1982).
24. A. W. Knight, G. M. Greenway, *Analyst* **119**, 879 (1994).
25. M. Shim, P. Guyot-Sionnest, *Nature* **407**, 981 (2000).
26. C. Wang, M. Shim, P. Guyot-Sionnest, *Science* **291**, 2390 (2001).
27. T. Makimura, Y. Kunii, N. Ono, K. Murakami, *Appl. Surf. Sci.* **127–129**, 388 (1998).
28. H. C. Choi, J. M. Buriak, *Chem. Mater.* **12**, 2151 (2000).
29. The support of this research by grants from NSF and the Robert A. Welch Foundation is gratefully acknowledged. Thanks to P. Barbara, F. R. Fan, and M. Buda for helpful discussions.

26 December 2001; accepted 3 April 2002

Global Azimuthal Anisotropy in the Transition Zone

Jeannot Trampert^{1*} and Hendrik Jan van Heijst²

Surface wave dispersion measurements for Love wave overtones carry evidence of azimuthal anisotropy in the transition zone of Earth's mantle (400 to 660 kilometers deep). A Backus-Gilbert inversion of anisotropic phase velocity maps, with resolution kernels mainly sensitive to the transition zone, shows a robust long-wavelength azimuthally anisotropic velocity structure. This observation puts new constraints on the mineralogy and dynamics of the transition zone because this anisotropy may result from aligned minerals, tilted laminated structures, or even organized pockets of fluid inclusions.

The nature of the transition zone has always been central to understanding the dynamics of Earth's mantle. Our inferences on the thermal and chemical evolution of Earth depend largely on whether the transition zone is due to pressure-induced phase changes and/or compositional variations of minerals (1). All seismic investigations of transition zone structure assume isotropic velocities. Seismic anisotropy is recognized as a good indicator of deformation and mantle flow (2, 3), but is mainly observed in the uppermost mantle (4). Particularly in the transition zone, the observation of anisotropy is difficult because fundamental mode surface waves have most of their sensitivity above the transition zone and the bulk of teleseismic body waves, below. Nevertheless, an indication of radial anisotropy around the 660-km discontinuity was found by reconciling observations of body wave travel times and free oscillation frequencies with a spherically symmetric model (5). Indications of localized azimuthal anisotropy near the same depth are inferred from compressional (P) to horizontal shear (SH) wave conversions (6, 7). Some observations of mainly S wave splitting require anisotropy in the upper transition zone (400 to 520 km) (8) and just below the 660-km discontinuity (9).

It recently became possible to make automatic surface wave overtone phase velocity measurements from millions of seismograms (10). These data are ideally suited for studying the transition zone because of their peak sensitivity in this depth range. Theory indicates (11,

12) that a slightly anisotropic medium causes an azimuthal dependence of local phase velocities of Love and Rayleigh surface waves as follows

$$\frac{dc}{c}(\omega, \psi) = \alpha_0(\omega) + \alpha_1(\omega) \cos(2\psi) + \alpha_2(\omega) \sin(2\psi) + \alpha_3(\omega) \cos(4\psi) + \alpha_4(\omega) \sin(4\psi) \quad (1)$$

where dc/c is the relative phase velocity perturbation with respect to a spherically symmetric reference Earth model, ω is the radial frequency, and ψ is the azimuth along the path. It can be shown that the $\alpha_i(\omega)$ are local vertical averages of 13 independent linear combinations of specific elements of the stiffness tensor (13). $\alpha_0(\omega)$ corresponds to the average over all azimuths and describes transverse or radial anisotropy involving the well-known Love parameters A, C, F, L, and N (14). The 2ψ and 4ψ terms involve an additional eight parameters that describe the azimuthal variations of A, F, L, and N. To make robust inferences of anisotropy, we chose to use Love wave overtones only [see Methods in Supporting Online Material (SOM)], where the 2ψ and 4ψ terms depend on one elastic parameter each, referred to as G and E, respectively (13).

We selected more than 100,000 Love wave measurements for minor and major arc paths corresponding to the first and second overtone branch (see Methods in SOM). The minor arc is the great circle angular distance between source and receiver, and the major arc is its complement. The path averaged phase velocity measurements are used to derive models of azimuthal anisotropy specified by the coefficients $\alpha_i(\omega)$ (see Methods in SOM). Fundamental mode phase data cannot easily distinguish between isotropic and anisotropic models (15, 16)

because of the uneven local azimuthal coverage, which is responsible for tradeoffs between the different $\alpha_i(\omega)$. We designed a technique based on relative weighting, which finds the optimal amount of azimuthal anisotropy for a given data set (see Methods in SOM), and we constructed phase velocity models based on Eq. 1. Toroidal overtone measurements are more difficult to make than spheroidal ones and have not previously been used for inferring three-dimensional (3D) Earth structure. Apart from strict quality checks on the data (17), the original measurement technique (10) has been extended to major arcs, which makes the overtone separation easier due to a longer distance of propagation. We further compared the isotropic part of our constructed phase velocity maps with those predicted from the 3D velocity model S20RTS (18). This model did not use any Love wave data, and the predictions can thus be used as an independent quality check of our measurements. For all selected overtones, the correlation (up to spherical harmonic degree 20) between our $\alpha_0(\omega)$ maps and the S20RTS predictions ranged from 0.75 to 0.80 with bootstrap confidence levels (19) higher than 99%. These high correlations corroborate the effectiveness of the measuring technique to separate overtones.

The anisotropic phase velocity models specify at each point on Earth's surface the local depth averages of the anisotropic parameters G and E that describe the 2ψ variation of the vertical shear velocity (SV) and the 4ψ variation of the SH velocity, respectively. The depth kernels are calculated in a spherical Earth (16, 20) (fig. S1). At a given depth, G and E are calculated from the secondary data $\{\alpha_i(\omega)\}$ and the kernels. This represents a linear inverse problem, and the most general solution is to construct models as a linear combination of the data themselves. We opted for a Backus-Gilbert approach (21), where the resolution of the model itself is optimized toward a desired shape (see Methods in SOM). For our given overtones, we were able to find a set of coefficients that give resolution kernels mainly sensitive to the transition zone (Fig. 1). These resolution kernels show that most structure above and below the transition zone cancels out; i.e., a synthetic test with data derived from a target model above or below the transition zone would retrieve an almost zero model, whereas a target in the transition zone would be fully recovered. Such a Backus-Gilbert inversion represents a test of whether or not anisotropy is present in the transition zone.

¹Faculty of Earth Sciences, Utrecht University, Post Office Box 80021, 3508 TA Utrecht, Netherlands.

²Shell International Exploration and Production, Post Office Box 60, 2280 AB Rijswijk, Netherlands.

*To whom correspondence should be addressed. E-mail: jeannot@geo.uu.nl.